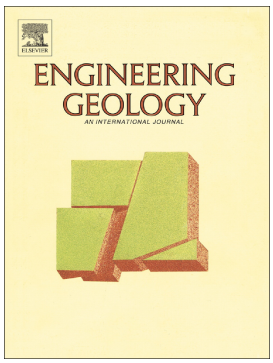

Characterizing and monitoring a high-risk sinkhole in an urban area underlain by salt through non-invasive methods: Detailed mapping, high-precision leveling and GPR

Jorge Sevil, Francisco Gutiérrez, Carlos Carnicer, Domingo Carbonel, Gloria Desir, Ángel García-Arnay, Jesús Guerrero

PII: S0013-7952(19)32321-X

DOI: https://doi.org/10.1016/j.enggeo.2020.105641

Reference: ENGEO 105641

To appear in: *Engineering Geology*

Received date: 11 December 2019

Revised date: 21 March 2020

Accepted date: 14 April 2020

Please cite this article as: J. Sevil, F. Gutiérrez, C. Carnicer, et al., Characterizing and monitoring a high-risk sinkhole in an urban area underlain by salt through non-invasive methods: Detailed mapping, high-precision leveling and GPR, *Engineering Geology* (2019), https://doi.org/10.1016/j.enggeo.2020.105641

Characterizing and monitoring a high-risk sinkhole in an urban area underlain by salt through non-invasive methods: detailed mapping, high-precision leveling and GPR

Jorge Sevil[a,*] jorgesevil@unizar.es, Francisco Gutiérrez[a], Carlos Carnicer[a], Domingo Carbonel[a], Gloria Desir[a], Ángel García-Arnay[a], Jesús Guerrero[a]

[a]Departamento de Ciencias de la Tierra, Universidad de Zaragoza, C/. Pedro Cerbuna 12, 50009 Zaragoza, Spain

[*]Corresponding author.

Abstract

Two critical aspects for assessing the hazard and managing the risk associated with active sinkholes in developed areas are the precise mapping of the areas affected by ground instability and the quantitative characterization of the ground displacement (kinematic style, spatial-temporal patterns, rates). However, sinkhole site investigations typically provide a static picture of the instability phenomena, and the performance of remediation measures is rarely evaluated using time-series of displacement. This work illustrates the practicality of a non-invasive approach, combining detailed mapping, ground penetrating radar (GPR), and high-precision leveling, for the characterization at different time scales of the ground deformation associated with an active sinkhole in an urban area. The selected highly-active sagging and collapse sinkhole affects four multi-storey buildings in Zaragoza city, Spain, involving direct losses higher than 15 Meuro. GPR data provided information on the internal structure of the sinkhole and the subsidence mechanisms. The boundaries of the ground-deformation zone, established with the GPR data, and especially high-precision leveling, indicate a sinkhole area two times larger than that proposed on the basis of airborne imagery and surface deformation features (length from 100 m to 130 m). The leveling profiles reveal an inner rapidly subsiding

zone with vertical displacement rates as high as 3 cm/yr, an outer slow settlement ring, and a marginal uplifting bulge with vertical displacement rates that reach 0.6 cm/yr. This marginal bulging processes is probably a relatively common process in sagging sinkholes, which may have gone unnoticed since its identification requires the use of geodetic methods with utmost accuracy, such as high-precision leveling. Monitoring data indicate that ongoing salt dissolution significantly contributes to the active subsidence and reveal the high impact on the subsidence of water pumping from the evaporitic aquifer and the limited efficiency of a shallow compaction grouting program performed above cavities and karstification zones.

Keywords: sinkhole mapping; deformation rings; subsidence; uplift; strain rates; geophysics.

1. Introduction

Active sinkholes in urban areas may pose severe risk situations with considerable economic and societal implications. Subsidence related to individual or multiple sinkholes may result in the destruction of buildings (e.g. Jassim et al., 1997; De Bruyn and Bell, 2001; Dougherty, 2005; Fischer et al., 2018) and the evacuation of a significant number of people (Goodings and Abdulla, 2002). For instance, ground deformation related to salt dissolution led to the abandonment of Puilatos village in the Gállego River valley, NE Spain (Zarroca et al., 2017). At Maohe village, China, a heavy rainfall event triggered 41 sinkholes damaging 143 houses (69 collapsed) and forcing the relocation of 1,830 people (Lei et al., 2013). Catastrophic collapse sinkholes may also result in life losses. In the Far West Rand of South Africa, collapse sinkholes mainly induced by dewatering of dolomite aquifers for gold mining have caused a total of 39 fatalities (Heath and Constantinou, 2015). In Seffner, Florida, a person was suddenly entombed within a sinkhole that opened beneath his bedroom while he slept in 2003 (Witze, 2013).

The impact of subsidence damage is particularly important in the mantled evaporite karst of Zaragoza city and its environs, which is considered to be the area in Europe with the highest sinkhole risk (Gutiérrez et al., 2018). Here, most of the sinkhole-related problems and losses are associated with pre-existing active dolines that were buried by anthropogenic deposits and used for construction (e.g., Galve et al., 2015). Obviously, in this context, the most effective mitigation strategy is the designation of sinkholes and its marginal areas, established through a set-back distance, as no-build zones (preventive planning) or zones that require special investigations and construction designs (e.g., Gutiérrez et al., 2018 and references therein). The application of these measures requires the precise mapping of the existing sinkholes and areas affected by ground deformation. The production of these detailed maps typically faces challenging circumstances in urban and periurban areas: (1) lack or limited of geomorphic expression of the depressions due to human alterations (e.g., infill, construction); (2) constraints imposed by urban elements for the application of some investigation methods and their distribution, particularly intrusive ones (e.g., trenches, boreholes; Sevil et al., 2017); and (3) the geomorphic expression of the sinkholes may significantly underestimate (Pueyo-Anchuela et al., 2013; Gutiérrez et al., 2018) or overestimate (Fabregat et al., 2017) the extent of the area affected by ground deformation. An additional important information is the delineation of the areas affected by active deformation and the quantitative characterization of the ground displacement (sense of movement, rates, spatial-temporal patterns).

There is an increasing number of investigations that illustrate the practicality of multiple non-invasive techniques for the characterization of damaging sinkholes in urban areas, such as ground penetrating radar (De Giorgi and Leucci, 2014), electrical resistivity tomography (Gołębiowski and Jarosińska, 2019), reflection seismics (Wadas et al., 2017), time-lapse gravimetry (Kobe et al., 2019). However, these works are mainly focused on geometrical aspects and provide a static picture of the sinkholes, lacking critical information on the patterns

and rates of the active deformation phenomena. Moreover, there is also a significant number of works that describe remediation measures applied to active sinkholes, but they rarely asses their performance comparing pre- and post-remediation displacement measurements (e.g., Gutiérrez et al., 2019). This work illustrates through the investigation of an active sinkhole involving direct economic losses higher than 16 Meuro, how a relatively simple and easy-to-implement approach, including detailed mapping, GPR and high-precision leveling, can be used to obtain critical information on the ground deformation process at different time scales: (1) subsidence mechanisms; (2) boundaries of deformation zone, (3) spatial variability of deformation, including subsidence and marginal flexural bulging; (4) displacement rates; and (5) the impact of structural and non-structural mitigation measures.

2. Geological and geomorphological setting

The analyzed sinkhole is located in the mantled evaporite karst developed in the central sector of the Ebro Cenozoic Basin (e.g., Galve et al., 2009) (Fig. 1). This is the southern foreland basin of the Pyrenean orogen, which is drained longitudinally by the Ebro River. Here, this major fluvial system has excavated a broad and extensively alluviated valley into the sub-horizontally lying evaporitic Zaragoza Gypsum Formation (Quirantes, 1978). This is an Oligo-Miocene continental succession more than 850 m thick deposited in an extensive high-salinity playa-lake system (Salvany et al., 2007). Only the upper 300 m of the formation are situated above the base-level of erosion (i.e., bottom of the Ebro Valley). Borehole data indicate that the evaporitic sections of this formation are composed of anhydrite ($CaSO_4$), halite (NaCl) and glauberite ($Na_2Ca[SO_4]_2$) (Salvany et al., 2007). However, the exposures of the outcropping upper part of the formation display secondary gypsum with interbedded marls and claystones (Salvany, 2009). This secondary gypsum occurs in the weathered near-surface zones, where halite has been dissolved and anhydrite and glauberite have been transformed into gypsum by hydration and incongruent dissolution, respectively (Salvany, 2009). The presence of hidden

high-solubility saline units plays an instrumental role in the development of dissolution and subsidence processes in the region (e.g., Guerrero et al., 2013; Acero et al., 2015; Desir et al., 2018). Halite and glauberite have much higher equilibrium solubilities (360 and 118 g/l, respectively) than gypsum (2.4 g/l) (Ford and Williams, 2007).

Unfortunately, the site has not been investigated by boreholes deep enough to gain information on the lithostratigraphy of the primary unweathered evaporitic succession underlying the sinkhole. Nonetheless, a thorough deep-borehole investigation carried out by Salvany (2009) to appraise glauberite deposits 5-15 km south of the Estrellas sinkhole provides clues on the stratigraphic position of the bedrock underlying the site. This author differentiated three lithostratigraphic units in the upper part of the Zaragoza Formation, in ascending order: (1) Lower Halite Unit, which thickens towards the Ebro Valley and reaches 75 m in thickness in the area investigated by Salvany (2009); (2) Intermediate Glauberite Unit, 150-175 m thick, comprising seven evaporitic cycles of brown-grey clay, anhydrite, glauberite and halite that record the expansion of the evaporitic lake; (3) Upper Anhydrite Unit around 250 m thick and mainly consisting of nodular anhydrite. The Estrellas sinkhole occurs on a terrace of the Ebro River lying at 237 m a.s.l. and the base of the alluvial cover, around 35 m thick, is situated at approximately 200 m a.s.l. In a borehole drilled 7 km to the south (A5 borehole), the contact between the Lower Halite Unit and the Intermediate Glauberite Unit is situated at 175 m a.s.l. (Salvany, 2009; Fig. 1B). Considering the general subhorizontal attitude of the bedrock, this indicates that the Quaternary alluvium at the Estrellas sinkhole site is underlain by the following evaporitic sections and/or residual deposits (karstic residue) related to their dissolution: the upper part of the Lower Halite Unit, or the lower part of the Intermediate Glauberite Unit, which includes the thicker glauberite beds of the unit, as much as 30 m thick (Salvany, 2009). This is also supported by a borehole drilled 2 km to the north (Miralbueno borehole), which encountered a halite section 90 m thick below 110 m a.s.l., overlain by a

succession 100 m thick including karstic residue and terrace alluvium (Salvany et al., 2007; Fig. 1B).

The entrenchment and northward migration of the Ebro River into the evaporitic Zaragoza Formation has resulted in an asymmetric valley, which shows a prominent linear gypsum escarpment along its northern margin, and a stepped sequence of terraces and pediments on the opposite side. Guerrero et al. (2013) mapped a total of 11 terraces in this sector of the Ebro Valley, with the oldest terrace situated at 200-210 m above the current channel. Figure 1C shows the location of the Estrellas sinkhole within its geomorphological context. It lies on terrace T4, situated 40 m above the river channel. The terrace deposits in this sector of the valley show significant local thickenings related to dissolution-induced synsedimentary subsidence, locally reaching more than 50 m (Guerrero et al., 2013). The terraces are dissected by a poorly-ranged network of flat-bottomed infilled valleys. The alluvial surfaces are riddled by sinkholes that locally control the path of drainages or disrupt them acting as swallow holes. There seems to be two morphologic end-members among these karstic depressions (Gutiérrez et al., 2009): (1) subcircular sinkholes commonly less than 100 m in diameter and well-defined scarped edges; (2) elongated or irregular subsidence depressions hundreds of meters long with vague edges.

3. History of the sinkhole

The oldest graphic document in which the Estrellas sinkhole can be identified is a grey-scale photogrammetric orthoimage produced for the Ebro Basin Water Authority in 1927 (Fig. 2A). The sinkhole is captured with relatively low resolution as a dark (i.e., vegetated) subcircular feature ca. 50 m across on a bare terrace surface. It is also observable in aerial photographs from 1946 and 1956 (American flights A and B). The images of the latter flight, with higher resolution, allow the interpretation under the stereoscope of a complex NW-SE-oriented

depression around 100 m long (Fig. 2B). The NW sector displays a nested, scarp-edged depression 60 m in diameter with tree vegetation. The SE sector shows a vague edge defined by a subtle slope break, and a gentle NW inclination. These morphological features reveal an overall asymmetric deformation pattern, with much higher subsidence in the NW half of the sinkhole. In 1962, a factory was built overlapping the NE sector of the sinkhole (Fig. 2C). This structure suffered from severe subsidence damage immediately after its construction, including the sudden occurrence of a collapse sinkhole 5 m across and 3 m deep (Gutiérrez et al., 2009). Measures applied to ameliorate the subsidence problems included piling with an insufficient depth of 18 m and the removal of the portion of the factory affected by settlement. Figure 2C shows the resulting gap and a band of dark asphalt cover on the pavement mantling the marginal scarps and fissures of the sinkhole. In 1996, after the demolition of the factory, a company (ENTECSA) carried out a geotechnical survey at the sinkhole site to advice for the construction of several buildings. The geotechnical company recommended to found the structures in the sinkhole area with deep piles or to avoid the sinkhole. They produced a map of the outline of the sinkhole as defined by marginal scarps and fissures, showing a slightly elongated subsidence feature with a 100 m long major axis following a WNW-ESE orientation. The proposed perimeter of the sinkhole has been georeferenced and depicted on a recent orthoimage (Fig. 2D). The Estrellas sinkhole was also inventoried and mapped at a 1:5,000 scale in a report on flooding and subsidence hazards (Simón et al., 1998), which was incorporated in the general land-use plan of Zaragoza city and approved by the city Council in 1999 (Fig. 3).

In 1997 a department store was constructed overlapping the northern sector of the sinkhole (building A in Fig. 2D) with a combined foundation design: (1) pads outside the sinkhole area mapped by ENTECSA in 1996; and (2) piles within the sinkhole as much as 65 m deep and with decreasing depths towards the sinkhole edge, based on the assumption that the subsidence structure is controlled by inward dipping failure planes. For the construction of the piles, a

large excavation more than 20 m deep was performed in the sinkhole area. The cuttings of the pit exposed a gravelly terrace deposit affected by (1) a basin structure with centripetal dips; (2) a master inward dipping fault juxtaposing terrace deposits against an anthropogenic fill; and (3) secondary synthetic and antithetic faults, some of which reached the ground surface (Gutiérrez et al., 2009). This department store has been barely affected by deformation, whereas the adjacent ground experiences continuous and rapid subsidence (Fig. 3).

The multi-storey apartment building D was constructed with pad foundation in 2001 south of the sinkhole area mapped in 1996 (Fig. 2D). However, the building shows cracks and dilated joints in its northern sector coherent with subsidence related to the Estrellas sinkhole.

The construction of building C was finished by the end of 2002, with its western sector overlapping the sinkhole area (Fig. 2D). This building was founded on alluvium with pads and continuous strip footings along the outer wall. The above-foundation structure comprises five blocks separated by four transverse expansion joints (form east to west, blocks C1 to C5; Fig. 3). Soon after the occupation of the building in 2003, rapid toppling and settling of block C5 towards the sinkhole center was detected, creating alarm among the owners. This led to the implementation of a monitoring program mainly focused on the deformation of the building, especially the expansion joints. Up to the present time, the whole building has been affected by deformation, essentially accommodated along the expansion joints and with no significant disturbance within the blocks that behave as semi-rigid bodies. All the joints are affected by horizontal separation that increases from the base to the rooftop of the building and decreases from west to east. In 2007, a report on the condition of the structure produced for the City Hall indicated that some pillars had reached 70% of their acceptable eccentricity (10.2 cm) before failure initiation. By that time the upper part of the westernmost block C5 had experienced a horizontal displacement at the top of 7.1 cm.

In 2007, the pumping station located in the vicinity of the sinkhole, south of building C (Fig. 3), was closed down and irrigation of the green areas was stopped to prevent their potential adverse effects on the sinkhole activity. In 2008, the alluvial deposits underlying the footprint of building C were subject to a compaction grouting program from the basement at a cost of 1.3 MEuro. This measure was aimed at improving the mechanical properties of the soil overlying the karstified bedrock. A cement-bentonite grout was injected up to depths of 15 m (blocks C4, C5) and 12 m (blocks C1 to C3) (Fig. 3). In 2012, the green area of the square situated in the central sector of the sinkhole was covered by a wedge-shaped and S-sloping clay cap to reduce water infiltration. The owners of the flats started a lawsuit in 2008 requesting for a compensation equivalent to the appraisal price of the property (ca. 15 MEuro), arguing that the planners gave permission for the construction of a building with shallow foundations in an area with a well-known active sinkhole.

Building B was constructed in 2005, with its NE corner overlapping the sinkhole (Fig. 2D). This portion of the structure was founded with a thick slab of reinforced concrete. The paved surfaces adjacent to the NE corner of the building show evidence of significant subsidence, whereas the building apparently remains undisturbed, indicating that the structure is in a cantilever situation, with the base of the undermined rigid slab detached from the settled ground.

4. Previous investigations

The Estrellas sinkhole and the groundwater of the pumping well situated in its vicinity have been analyzed in previous investigations. Gutiérrez et al. (2009) characterized the sinkhole on the basis of boreholes drilled by several geotechnical companies, limited shallow geophysical data (ERT and GPR), and two trenches (Fig. 3). Four lithostratigraphic units where differentiated in the borehole logs in descending order: (1) Anthropogenic and sinkhole-fill

deposits, that reach around 6 m in the NE sector of the sinkhole, where the nested collapse depression was located (boreholes B1 and B2 in Fig. 3). (2) Terrace alluvium 28-35 m thick consisting of slightly cemented gravels with interbedded fine-grained beds. The base of the alluvial cover drops as much as 9 m from the margins to the center of the sinkhole (from 28 m to 37 m below the ground surface). (3) A residual material 7-38 m thick consisting of unstratified dark gray clay and gypsum with large cavities ascribed to a residue related to the karstification of the bedrock and collapse breccias. This unit reaches 28.3 m and 37.9 m in thickness in boreholes B3 and B4 (Fig. 3), and in the latter one voids with an aggregate length of 10.1 m were identified between 45-63 m depth. (4) Solid bedrock, described as stratified gypsum with interlayered marls and cavities as much as 1.6 m high. The depth to the top of the bedrock varies from 37 m in the marginal sector of the sinkhole (boreholes B5, B6, B7 in Fig. 3) to unknown depths below 65 and 71 m in the central sector of the sinkhole (boreholes B3 and B4, respectively). Unfortunately, the lithology of the evaporites and the potential presence of salts is poorly known since few boreholes reached the bedrock and none of them was drilled with brine to prevent the dissolution of halite or glauberite beds. The water table was measured in those boreholes at 37-37.5 m, close to or below the base of the detrital cover, which functions as a perched alluvial aquifer connected with the underlying evaporitic karst aquifer.

Gutiérrez et al. (2009) investigated two trenches restricted to the green area of the central square, one excavated across a scarp on the SW sector of the sinkhole (Trench SW) and another one within the sinkhole in the SE sector (Trench SE) (see location in Fig. 3). The main findings derived from the trenches, mainly Trench SW, include: (1) The structural style indicates that subsidence in the Estrellas sinkhole is accommodated by both collapse (discrete dip-slip displacement on steep faults) and sagging (spatially continuous passive bending of the cover), and consequently it can be classified as a cover and bedrock collapse and sagging sinkhole. (2) Trench SW together with GPR profiles showed that sediments located beyond the fault scarp

(i.e., footwall) that apparently defined the edge of the sinkhole are affected by fissuring and inward tilting, revealing that the buried sinkhole and the subsidence area have a larger extent. (3) Minimum average displacement rates of 1.2-1.8 cm/yr were estimated for the oversteepened faults exposed in Trench SW considering the throw of anthropogenic deposits and their maximum age.

Pueyo-Anchuela et al. (2012) analyzed the distribution of deformation features observed at the surface and interpreted from GPR data and concluded that the extent of the sinkhole was underestimated in previous works (e.g., ENTECSA, 1996; Simón et al., 1998). Acero et al. (2013, 2015) carried out a hydrochemical investigation in the Ebro River valley to gain insight into the hydrogeology of the interconnected evaporite-karst and alluvial aquifer system and the associated dissolution processes involved in the development of sinkholes. The geochemical calculations were based on samples collected from numerous water points between January 2011 and January 2012, including the pumping well located next to the Estrellas sinkhole. According to Acero et al. (2015), this well used to withdraw water from the evaporitic aquifer at a depth of around 70 m for irrigation the green zones of the area. Water samples, with high ionic concentrations, showed a roughly constant hydrochemistry throughout the year, with the following average values relevant to this investigation: (1) TDS (Total Dissolved Solids): 2622 mg/l; (2) Electrical conductivity: 2834 µS/cm; (3) Ca: 650 mg/l; (4) Cl: 198 mg/l; (5) Na: 153 mg/l; (6) SO_4: 1552 mg/l. Saturation indexes calculated with the geochemical modelling software PHREEQC (pH-Redox-EQuilibrium in C language) indicated that the groundwater pumped from the evaporitic aquifer next to the Estrellas sinkhole is in equilibrium with gypsum and clearly unsaturated with respect to halite. This data indicates that the water that was used for irrigation in the sinkhole area did not have the capability to cause gypsum dissolution. Moreover, this groundwater has an average Na/Cl molar ratio of 1.2, suggesting that part of the dissolved Na could be derived from glauberite dissolution.

5. Methodology

5.1. Surface deformation mapping

The study area was investigated using aerial photographs from 1956 (American Flight B) and printed at a scale of 1:30,000. These grey-scale images allowed the identification under the stereoscope of the geomorphological features that existed before the urban expansion of Zaragoza city. The most useful aerial photographs were orthorectified and georeferenced with ArcMap 10.5 to produce the geomorphological map of Fig.1, which depicts the distribution of the sinkholes identified in these low-spatial-resolution and small-scale images. We also produced by direct surveying a map of surface deformation features of the sinkhole site using a 1:500 scale gridded orthoimage. This map illustrates the spatial distribution and dimensions of the deformations mainly observed on paved surfaces (e.g., scarps, fissures, tilting, buckling), as well as the date of occurrence of small collapses (Fig. 3). It should be noted that some paved surfaces affected by rapid deformation are frequently repaired, and consequently strain measurements provide minimum values. This detailed map was the basis for designing the layout of the coincident leveling lines and GPR profiles. The longest investigation line was located in the Estrellas Street in order to traverse the eastern and western edges of the sinkhole (Estrellas Sinkhole North). Two additional perpendicular lines were placed along the Algenib (Estrellas Sinkhole West) and Capella streets (Estrellas Sinkhole East) to cover the southwestern and southeastern edges, respectively. The northern sector is overlain by building A (Fig. 3).

5.2. High-precision leveling

A total of 10 leveling campaigns were carried out approximately every three months, from 24 January 2017 to 15 May 2019, covering 841 days. Relative vertical ground deformation was measured along three pre-installed lines by high-precision differential leveling using a digital

level (Leica DNA03), a tripod with wooden, fixed-length legs, and a 2 m-long bar-coded invar staff (Leica GPCL2) (see location in Figure 3). This equipment is characterized by an exceptional measuring accuracy with a standard deviation of 0.3 mm per kilometer in double-run leveling. The leveling lines, 85 to 200 m long, were installed with iron steel nails (HILTI X-NK 32 S12). These benchmarks were placed at a regular spacing of 5 m. The elevation difference between successive benchmarks was measured stationing the level at an intermediate position and taking backsight and foresight measurements in fore and back runs (backward-forward method based on double leveling). This procedure minimizes the errors related to refraction and the displacement of the collimation axis (ISO 17123-2, 2001), and allows the detection of misreadings. The values were considered valid if the difference between the foresight and backsight measurements was lower than 0.3 mm. The kilometric error is given by the difference between the summatories of the fore- and backsight measurements, divided by the square root of the line length in km. The errors calculated for the three lines are very low compared with the measured deformation rates. Following the methodology presented by Desir et al. (2018), profiles of cumulative vertical displacement were plotted by smoothed interpolation utilizing the first profile as datum. These data were used to calculate the following parameters with the appropriate profiles: (1) Number of benchmarks recording subsidence and length of the line clearly affected by settlement (subsidence section). (2) Mean cumulative subsidence and mean subsidence rate derived from the subsidence section of the line. (3) Maximum subsidence and maximum subsidence rate derived from the benchmark with highest negative displacement. (4) Asymmetry index, given by the ratio between the average subsidence recorded in the last profile on both sides from the highest subsidence point, with the highest value in the numerator. The higher the value, the higher the asymmetry of the cumulative strain. (5) Eccentricity index, computed by the ratio between the horizontal distance from the lowest point of the latest profile to the furthest edge of the subsidence section and the

length affected by subsidence. The higher the value, the higher the deviation of the maximum subsidence point from the center. A value equal to 0.5 indicates no eccentricity (i.e., maximum displacement in the center of the subsidence section). (6) Subsidence geometry index, given by the ratio between maximum cumulative subsidence and mean cumulative subsidence, both derived from the latest subsidence profile. This value would be 1 in a perfect piston-like collapse and 2 in a subsidence structure with the geometry of a perfect chevron fold (kink fold) in cross-section. Therefore, the closer the value to 1, the higher the deformation gradient at the margins of the subsidence structure and presumably, the higher contribution of the collapse mechanism.

5.3. Ground Penetrating Radar (GPR)

The leveling data provide quantitative information about vertical displacement of the ground, both subsidence and uplift, and its spatial-temporal variation over the monitoring period (i.e., instrumental record). In order to obtain subsurface information on the longer-term deformation that affects the sediments in the buried sinkhole located in an urban setting (i.e., geological record), we applied Ground Penetrating Radar (GPR). This is a non-invasive near-surface geophysical method commonly applied in sinkhole investigations (e.g., Zarroca et al., 2017; Ronen et al., 2019). The GPR system consists of a control unit, an antenna that transmits electromagnetic waves to the subsurface and a receiving antenna that records the time delay and the strength of the reflected waves. The characteristics of these reflections are related to changes in the electromagnetic impedance of the subsurface materials, providing information on stratigraphic and structural features associated with the investigated sinkhole (e.g., cavities, sinkhole fills, collapse faults, fissures, tilted beds, sagging structures) (Rodríguez et al., 2014; Zarroca et al., 2017). We acquired GPR profiles in July 2017 with a RIS system (IDS Ingegneria dei Sistemi) coinciding with the leveling lines for direct comparison (Fig. 3). The GPR profiles were replicated with 100 and 200 MHz shielded antennas that provide variable

penetration depth and resolution. The GPR data were processed with ReflexW v.8.2.2 (Sandmeier Scientific) through the following steps: (1) one-dimensional dewow to eliminate low frequencies; (2) time-zero correction to define the air/ground waves and eliminate early signals; (3) manual time-varying gain to amplify late travel-time signals; (4) background removal and bandpass frequency filter to remove undesired noise including system ringing and multiples; (5) topographic correction using the closest leveling data to the GPR acquisition date (20 July 2017). The time-to-depth conversion was performed using a single velocity of 0.1 m/ns derived from common midpoint data acquired in the vicinity of the sinkhole site (Rodríguez et al., 2014).

6. Results

6.1. Deformation on the ground and building C

The ground surface shows multiple evidence of active deformation (i.e., scarps, fissures, tilting, sagging, buckles, small collapses) (Figs. 3 and 4). The overall concentric distribution of the surface deformation features and their sense of displacement are clearly coherent with the Estrellas sinkhole; vertical and horizontal separation, as well as tilting towards the sinkhole center. The outermost deformation features define a subsidence structure interrupted in building A, founded with deep piles. This subsidence structure with recognizable surface expression has an approximately 102 m long and N85E oriented major axis and a 92 m long and N07W minor axis.

The most conspicuous deformation occurs in the paved surfaces adjacent to buildings A and B, designed with special foundations and apparently unaffected by subsidence. Nonetheless, building A shows cracking in the façades and the basement attributable to the sinkhole activity. The surfaces next to these buildings display sagging and tilting, with dips as high as 13°, and the sidewalks show significant vertical and horizontal separation from the base of their outer

walls (Fig. 4B, E). The paving stones of the northern sidewalk of the Estrellas Street display a contractional buckle attributable to compression in the axial part of the sagging structure. The SW corner of the clay cap in the central square, placed in 2012, and the adjacent sidewalk are affected by a conspicuous scarp. Building D shows arcuate dilated cracks on its eastern and western walls with the concavity facing towards the sinkhole center. In addition to the nested collapse documented in 1985, we have recorded two decimetre-scale collapse holes in the southern sector of the sinkhole (Fig. 3). The collapse of May 2015 may be related to a backfilled investigation trench with a poorly compacted fill (Fig. 4C) and the one occurred on June 2017 probably was the result of downward internal erosion (i.e., ravelling) of cover deposits along extensional fissures (Fig. 4D).

Building C, constructed with shallow foundations on the eastern sector of the sinkhole, is the most severely damaged structure (Gutiérrez et al., 2009) (Fig. 4A, F, and G). The monitoring of this building carried out by several companies since 2007 supplies, among other data, the relative displacement between moving blocks at the expansion joints.

The expansion joint between blocks C5 and C4 is the one affected by more rapid movement (Fig. 4A). This joint records a relative displacement, since both blocks are affected by deformation, although at different rates. Interestingly, its relative joint-normal displacement rate decelerated from 15.8 mm/yr (January 2003 – April 2007) to 7.8 mm/yr (April 2007 – October 2008) after the closure of the pumping well (April 2007), and to 5.0 mm/yr (November 2008 – 2018) following the shallow compaction grouting carried out beneath building C in 2008 (AMA and GEOCEC, pers. comm.). The rest of the expansion joints are also affected by relative displacement, although at slower rates. The joint-normal dilation measured from 2009 to 2018 yields relative displacement rates of 5.6 mm/yr, 2.47 mm/yr, 2.25 mm/yr and 0.68 mm/yr at joints C5-C4, C4-C3, C3-C2 and C2-C1, respectively. These joints show an overall steady displacement trend over this time interval overprinted by a secondary seasonal pattern,

with deceleration and acceleration in the summer and winter seasons attributable to thermal expansion and contraction cycles, respectively (AMA and GEOCEC, pers. comm.).

On August 2019, we took measurements in the rooftop of the building of the joint-normal and joint-parallel relative displacement accumulated since the construction of the building, 16.8 years ago (Figs. 3 and 4F). The joint-normal relative displacements at the expansion joints in the rooftop were 158 mm, 35 mm, 34 mm, and 15 mm for joints C5-C4, C4-C3, C3-C2 and C2-C1, respectively. Since at least blocks C5 to C2 are toppling to the west in a domino-like fashion, the measurement of the joint-normal relative displacement at the joint closest to the sinkhole center (C4-C5) provides a minimum deformation value. The net joint-normal westward displacement of block C5 at its top can be approximately estimated summing the displacements measured in all the joints, providing a strain value of 142.7 mm (i.e., eccentricity) and an average displacement rate of 8.49 mm/yr.

6.2. Leveling and GPR data

6.2.1. Estrellas Sinkhole North

The 200 m-long Estrellas Sinkhole North leveling line, with 41 fixed control points, traverses the sinkhole mapped in previous works approximately across its central sector and extends well beyond the proposed edges (Figs. 3, 5E, Table 1). This line covers the western sector of the sinkhole, which displayed a nested deeper depression in old aerial photographs (Fig. 2B). A total of 7 benchmarks, including the one that records the most rapid subsidence, were lost due to re-pavement works carried out between the two most recent measurements (Fig. 4E). Consequently, the last profile of cumulative displacement only covers a portion of the sinkhole. According to the last complete deformation profile, subsidence clearly affects to a 75 m-long section of the line (37.5%, between points 12 and 27). Subsidence sections, when stationary, are better defined as the time elapsed from the first measurement increases, since in the slow-

moving marginal areas a longer time is needed for the cumulative subsidence to exceed the error margin of the measurements (Desir et al., 2018). Cumulative displacement measured along this subsidence section yields mean and maximum subsidence values of 33.60 mm and 59.10 mm and mean and maximum subsidence rates of 16.38 mm/yr and 28.80 mm/yr, respectively. These last two parameters are rather constant since the fourth measurement (25/9/2017), when the edges of the subsidence section become clearer in the deformation profiles. The deformation pattern is markedly asymmetric (Fig. 5E, Table 1), with the greatest subsidence point displaced towards the western edge (eccentricity index of 0.81) and a much steeper deformation gradient on the western flank (asymmetry index of 1.15), in agreement with the geomorphic features observed in old airborne imagery. The subsidence geometry index of 1.76 points to a significant sagging component and is coherent with the deformation style observed on the ground surface.

Interestingly, the leveling measurements record slow but persistent uplift on both sides of the subsidence section. The mean and maximum cumulative uplift (6.07 mm and 12.14 mm), and the mean and maximum uplift rates (2.96 mm/yr, 5.91 mm/yr) derived from the last complete deformation profile are 4.7-4.9 times lower that the corresponding subsidence values. The edges of the sections affected by uplift are not clearly defined and the displacement rates apparently show higher temporal variability. This can be attributed to the lower displacement rates, the relatively short leveling record, and a higher impact of deformation processes non-related to the sinkhole (e.g., thermal expansion and contraction). Nonetheless, it is possible to differentiate two clear uplifting segments 30 m and 15 m long on the western and eastern sides of the subsiding segment, respectively (Fig. 5 A and E).

Four GPR profiles 200 m long were collected along the Estrellas street. Two of them were acquired with 100 MHz and 200 MHz shielded antennas coinciding with the leveling line, placed on the southern sidewalk. The other two were collected on the northern sidewalk, with

a lateral offset of 16 m with respect to the previous ones, and further away from the sinkhole center (Fig. 5A). Figure 5 only includes three of the processed profiles, for brevity. All the GPR profiles, especially the ones acquired along the southern side of the street, show two marginal sections adjacent to buildings B and C with numerous diffraction hyperbolas that obscure the radargrams, and a central sector that captures the internal geometry of the subsidence structure (Fig. 5B and C). This central sector displays an asymmetric synformal geometry with two high-deformation sections in the flanks expressed by laterally truncated reflections, and a collapse structure superimposed on the steeper western side of the synform. The eastern high-deformation section is 15 m wide and shows three segments (Fig. 5C); two lateral ones with reflections dipping towards the sinkhole center, and a central one below the asphalt with horizontal reflections that might correspond to multiples. To the east of this high-deformation section there seems to be also inward dipping reflections, although poorly defined and obscured by the diffraction hyperbolae. The western high-deformation section consists of a nested collapse around 30 m wide with an inner tight synform, whose hinge coincides with the leveling point that records the highest subsidence (Figs. 5B, D). The synthetic and antithetic collapse faults are expressed as vertically offset reflections and the synform by inward dipping reflections. In the central sector of the profile some shallow reflections at shallow depth (c. 0.5-0.75 m) display onlap relationships, which probably mark the base of the anthropogenic fill (Fig. 5B).

The profiles collected on the northern side of the street show a similar asymmetric synformal geometry, but with less defined high-deformation zones in the margins, probably because the higher obliquity between the orientation of the structures and the profile (Fig. 5D). Nonetheless, the 100 MHz profile clearly captures the nested collapse and synform associated with the steeper western limb. Interestingly, all the GPR profiles collected on both sides of the

street suggest the presence of a subsidence structure larger than the subsidence section identified by leveling.

6.2.2. Estrellas Sinkhole West

The 85 m-long Estrellas Sinkhole West leveling line, with 18 control points, covers partially the western sector of the sinkhole, including the nested depression identified in old aerial photographs (Figs. 3, 6A). Between the last and the penultimate leveling campaigns, four control points were lost in the northern portion of the line due to re-asphalting works. Consequently, the last complete cumulative deformation profile is the one corresponding to 5/2/2019, which records 742 days of vertical displacement (Fig. 6D, Table 2). The overall leveling record indicates that the whole line is affected by subsidence and located within the sinkhole. This has a twofold implication: (1) cumulative subsidence measurements should be considered as minimum values; and (2) the line does not allow the identification of the deformation limit. The last complete measurements yield mean and maximum cumulative subsidence values of 26.43 mm and 65.51 mm, and mean and maximum subsidence rates of 13.00 mm/yr and 33.20 mm/yr, respectively (Table 2). The latter, measured at point 13, is the highest rate recorded in this work. The mean subsidence rate has remained constant during the record period. Maximum subsidence rates also indicate steady deformation, except for three anomalous and non-valid measurements from 2017 at point 13 (Fig. 6D). The displacement profiles show two deformation zones: (1) an inner zone between points 8-9 and 18 with rapid and symmetric subsidence; and (2) an outer zone between points 1 and 8-9 with slow subsidence. Very likely a similar low deformation zone is located to the north of the line, below building A. The high horizontal strain gradient (i.e. steepening of the deformation profile) recorded around points 8 and 9 coincides with the location of a conspicuous and rapidly developing scarp depicted in the surface deformation map (Fig. 3). This leveling line does not include any section affected by uplift. This is attributed to the fact that the line, with insufficient

length to fully characterize the deformation pattern, is restricted to the portion of the sinkhole that experiences settlement.

The GPR profiles acquired along the Algenib street, with significant obliquity with respect to the orientation of the structures, provide limited information on the subsurface geometry of the sinkhole. The 100 MHz profile (Fig. 6B) has better quality than the 200 MHz profile (Fig. 6C); higher penetration and less diffraction hyperbolas and undesired noise (i.e., system ringing and multiples). The underground reflections partially display a gentle synform locally affected by collapse faults. The most conspicuous one is a steep antithetic fault whose location coincides with that of a recent scarp depicted in the surface deformation map (Fig. 6). The fault responsible for the conspicuous scarp mapped between the leveling points 8 and 9 is not clearly captured in the GPR profiles. The southern portion of the 100 MHz profile, adjacent to building D shows some onlaps and upward fault truncations, probably related to the interface between the slightly cemented terrace deposit and the man-made ground.

6.2.3. Estrellas Sinkhole East

The 95 m-long Estrellas Sinkhole East leveling line, with 20 control points, is placed on the eastern sector of the sinkhole, which displays in old aerial photographs a poorly defined edge (Figs. 2, 3). All the benchmarks of this line remained in place throughout the measuring time span, covering 841 days (2.3 years). The subsidence section of the line extends along 65 m, from points 7 to 20 (Fig. 7D). The latter point could not be measured from 16/03/2018 to 12/02/2019 due to the presence of obstacles. In addition, neither the leveling profile (Fig. 7D) nor table 3 consider the benchmark placed at 55 m as it provides erratic values probably related to poor fixing with the ground (i.e., loose nail). The last measurements have yielded mean and maximum cumulative subsidence values of 3.18 mm and 5.79 mm, and mean and maximum subsidence rates of 1.38 mm/yr and 2.51 mm/yr, respectively. Both the mean and maximum

subsidence rates show limited variability, pointing to continuous and constant ground settlement. Similarly to the West line, the deformation profiles show an outer slow-subsidence sector between points 6 and 11, and an inner portion with higher subsidence rates. The sinkhole extends beyond the leveling line to the north, beneath building A, and consequently no geometrical indexes have been calculated. This line also records slow and persistent uplift along a 5 m long portion south of the subsidence section. The last measurements indicate mean and maximum cumulative uplift values of 1.01 mm and 2.28 mm, and corresponding rates of 0.44 mm/yr and 0.99 mm/yr, respectively. These latter rates are 2.13 and 2.54 times lower than the mean and maximum subsidence rates derived from this line.

Like in the western investigation line, the 100 MHz profile has better quality than the 200 MHz one, which shows laterally continuous surface multiples that obscures the profile and two large diffraction hyperbolae associated with the edges of building C (Fig. 7B, C). The lower part of the 100 MHz profile displays an asymmetric synform with a steeper northern limb. The reflections that define this synform locally show lateral truncations and associated abrupt dip changes, attributable to the presence of collapse faults. These deformed lower reflections, ascribable to terrace deposits, are unconformably overlain by more laterally continuous reflections, although also affected by some disruption, which may correspond to the anthropogenic fill.

7. Discussion

Active sinkholes in urban areas may create high-risk situations with significant social and economic implications, as illustrates the Estrellas sinkhole. Here, rapid and persistent subsidence severely damages a multi-storey building constructed on and next to a previously known sinkhole, leading to a >1.3 Meuro remediation program and a lawsuit resulting in an expected compensation to the owners of around 15 Meuro. Proper pre- and post-development

risk management at sinkhole sites, including hazard avoidance via preventive planning, requires gaining information about several relevant aspects, including: (1) limits of the area affected by deformation; (2) kinematic style of the strain (continuous versus episodic); (3) rate and sense of the deformation and its spatial-temporal patterns; and (4) dissolution and subsidence mechanisms. Monitoring the sinkhole-related deformation gains importance when remediation measures are applied, since they provide objective data for evaluating their performance and cost-effectiveness (Gutiérrez et al., 2019).

The investigation of sinkholes in urban areas pose two main limitations: (1) restrictions for the application of invasive methods (e.g., boreholes, trenching), and (2) obliteration of the geomorphic expression of the sinkhole by anthropogenic filling and construction. Nevertheless, buildings and pavements may help to assess and monitor the deformation related to the sinkhole activity in two different ways. On the one hand, human-built structures may be used as strain markers that allow mapping and measuring the cumulative deformation occurred since their construction and calculating average deformation rates. On the other hand, these artificial structures may offer an adequate scenario for the application of some monitoring techniques (e.g., Intrieri et al., 2015; Kersten et al., 2017; Benito-Calvo et al., 2018). In this case study, the deformation related to the Estrellas sinkhole has been characterized using various methods that can be categorized into three groups, according to their temporal scale: (1) mid-term deformation in human structures and the ground developed over a period of more than 15 years, that allows assessing the performance of mitigation measures; (2) short-term displacement over a period of around 2.3 years in paved areas recorded by high-precision leveling, that provides information on the current deformation; and (3) long-term deformation recorded in the subsurface deposits and identified using GPR.

7.1. Mid-term deformation

A monitoring program focused on the deformation of building C and its adjacent ground was initiated soon after the recognition of severe subsidence in this building. The relative displacement of the expansion joints of building C (Fig. 3), notably the joint situated closer to the sinkhole center (C4-C5), shows two drops in the deformation rate that coincide with the application of mitigation measures:

- In 2007, the joint-normal displacement decreased from 15.8 mm/yr to 7.8 mm/yr after the closure of the well situated at 20 m to the south of the building, revealing that groundwater pumping had a significant adverse impact on the subsidence problem. This well 70 m deep used to withdraw a large amount of water from the evaporitic aquifer to irrigate numerous green areas in this sector of the city. The cone of depressions created by groundwater pumping may accelerate the activity of sinkholes through different mechanisms (Gutiérrez et al., 2014): (1) buoyancy loss in the sediments situated above cavities and karstification zones, enhancing subsidence activity; (2) increased groundwater circulation, which may accelerate dissolution processes especially in salt-bearing evaporitic bedrocks. The latter mechanism may have played a significant role in the Estrellas sinkhole as discussed below.
- A second more limited drop in the displacement rate at the joint, from 7.8 mm/yr to 5.0 mm/yr, was recorded after the compaction grouting performed below the building. These data strongly suggest that this costly remediation measure, applied in the alluvium up to depths of 15-12 m, well above the karstified and cavernous bedrock situated below 37 m depth, had a limited contribution for the improvement of the stability conditions. In some active sinkholes of the Ebro Valley, monitoring data demonstrate that compaction grouting applied above the cavities and karstification zones may promptly accelerate and expand subsidence activity (e.g., Gutiérrez et al., 2019).

During our investigation we produced a surface deformation map of the Estrellas sinkhole, which was used as the basis for the subsequent GPR and leveling surveys. The overall

distribution of the deformation features indicates a subcircular subsidence structure 102 m long, similar in size to the depression interpreted in old aerial photographs taken before the infill of the sinkhole (ca. 100 m long) and the sinkhole boundary mapped in 1996 by topographic surveying using surface ruptures (ca. 100 m long). The new map has revealed that building D is also affected by subsidence damage, and that the NE corner of building B, founded with a thick reinforced slab in that sector must be in a cantilever situation, which may expand by undermining (Fig. 3).

7.2. Ground Penetrating Radar

Ground Penetrating Radar (GPR) is generally a suitable subsurface investigation technique for investigating sinkholes in urban areas. It is a non-invasive method applicable without major restrictions that allows identifying buried sinkholes with no geomorphic expression (e.g., Rodríguez et al., 2014; Gołębiowski and Jaroszewska, 2019). The use of unshielded antennas, typically with lower frequencies and higher penetration depth, was discarded because contamination from undesired reflections from above surface elements (e.g., buildings, trees, cables) were expected to mask the targeted subsurface features. The GPR profiles acquired with 100 MHz and 200 MHz shielded antennas capture the internal structure of the sinkhole recorded in the Quaternary alluvium at shallow depth (2.50-1.75 m depth), providing information on the subsidence mechanisms and approximate extent. The radargrams, in agreement with the interpretation of old aerial photographs and previous trenching investigations show (Gutiérrez et al., 2009): (1) an asymmetric sagging structure (i.e., synform) with stepper dips in the western sector; (2) collapse faults expressed as laterally truncated and vertically offset reflections; and (3) a nested collapse around 30 m wide at the western sector of the sinkhole superimposed in the hinge zone of the synform. These subsidence structures indicate that the Estrellas sinkhole can be classified as a cover and bedrock sagging-collapse sinkhole according to the genetic classification proposed by Gutiérrez et al. (2008, 2014).

The comparison of the GPR profiles with the surface deformation map offers the opportunity to identify some limitations of this geophysical technique. For instance, the collapse fault that produces a conspicuous and highly active scarp in the western investigation line was not clearly imaged in any of the GPR profiles (Fig. 6). Moreover, the sections of the profiles located next to the buildings are largely blurred by diffraction hyperbolae. This local information loss may be attributed to contamination produced by artificial elements (e.g., the walls of the buildings' basement, pipes, cables). In this investigation, the 100 MHz shielded antennas provided better quality radargrams than those obtained with the 200 MHz antennas. The former ones reach higher depths and show less small diffraction hyperbolae. Moreover, the GPR profiles acquired perpendicularly to the deformation structures (northern investigation line) offer more information on the subsidence structures than those with significant obliquity (eastern and western investigation lines). A similar result was obtained by Rodríguez et al. (2014) in the investigation of buried collapse sinkholes with a mesh of parallel GPR profiles.

GPR surveys with good spatial coverage may be used to map the boundaries of concealed sinkholes with well-defined collapse faults at their edges (Buurman and Reuther, 2006; Kruse et al., 2006). However, this task may not be feasible for sagging sinkholes in which their edges are defined by subtle and gradual changes in the dip of the strata (Gutiérrez et al., 2018) and even bulges with very limited structural relief. The GPR profiles collected in the Estrellas Street show a clear inner synform with relatively steep dips, and a marginal aureole with low-dipping strata. The resolution and quality of the GPR profiles is not good enough to precisely define the vague outer edge of this marginal low-deformation zone. Moreover, the dip of the reflections is affected by the topographic correction (Sandmeier, 2019), which in our case was carried out using leveling profiles with limited horizontal resolution (5 m) that do not capture local topographic changes such as scarp and local slope changes.

7.3. High-precision leveling

The presented data illustrates that the simple and relatively inexpensive high-precision leveling geodetic method (Kersten et al., 2017; Desir et al., 2018; Kobe et al., 2019) provides highly accurate data for characterizing the vertical displacements associated with active sinkholes over relatively short monitoring periods. This approach is particularly suitable for urban areas with paved surfaces that facilitate the installation of benchmarks. However, buildings and other human structures may impose significant constraints for the distribution of survey lines and may affect the persistence of the investigation points. The overall subsidence deformation recorded in the leveling lines shows good spatial correlation with the sagging structures imaged in the GPR profiles. For instance, the benchmarks that record the highest subsidence magnitudes and rates coincide with the hinge of the synforms imaged in the radargrams. This indicates concordance between the past and present-day subsidence and suggests temporal stationarity in the location of the deformation. Nonetheless, the leveling deformation profiles, constructed by the interpolation of point displacement data with a spacing of 5 m, do not have sufficient spatial resolution to capture discrete deformation structures such as the collapse faults identified in trenches, the GPR profiles and the surface deformation map. This shows the synergistic character of the different methods.

The leveling data has provided highly accurate information on the spatial distribution, magnitude and rate of vertical displacement, including a previously unrecognized subtle marginal bulging. The temporal evolution of the displacement indicates a continuous and steady deformation pattern, although the time span of the record is limited to 2.3 years. The northern and western leveling lines, which include the nested collapse structure identified in old aerial photographs and in the GPR profiles, yield the highest maximum (28.8 mm/yr and 33.2 mm/yr, respectively) and mean subsidence rates (16.38 mm/yr and 13.00 mm/yr, respectively) (Figs. 5 and 6; Tables 1 and 2). In contrast, the eastern leveling line, located in a marginal and vague area of the depression identified in old aerial photographs, record

significantly lower maximum and mean subsidence rates (2.5 mm/yr and 1.4 mm/yr, respectively) (Fig. 7D; Table 3). Moreover, this line records minimum displacement values since it does not extend beyond the deformation area of the sinkhole. The crossing lines installed in this investigation do not have common points at the intersection. However, such layout would allow to: (1) cross-check deformation values measured at the same point in two different lines; (2) assess the deviation between the measured displacement and the actual one in leveling lines that do not extend beyond the deformation zone and therefore record minimum vertical displacement values.

7.4. Marginal bulging

The North and East leveling lines record subtle uplift attributable to elastic flexure of the hardened cover (i.e., slightly cemented alluvium) induced by moment stresses transferred to the marginal area of the subsidence zone (Figs. 5 and 7; Tables 1 and 3). Therefore, ground displacement in the Estrellas sinkhole is characterized by an inner subsiding zone and an outer aureole affected by bulging. The boundary between these two domains, defined by a virtual no-displacement point in the deformation profiles, becomes clearer as the time span of the record increases and the cumulative deformation overwhelms the error margin of the measurements and potential displacements unrelated to the sinkhole activity. In the northern leveling line, the uplifting marginal sections have an aggregate length of 45 m, compared with the 75 m length of the subsidence section. The average uplift rates in this line are 4.7-4.9 times lower than the mean subsidence rate. The uplifting section in the eastern leveling line is 5 m long and shows a mean displacement rate 3.1 times lower than that of the incomplete subsidence section. To our best knowledge, this is the first time that marginal uplift has been characterized quantitatively in an active sinkhole. Previous works implicitly illustrate this apparently peculiar deformation pattern in active sinkholes through leveling deformation

profiles (Kersten et al., 2017; Desir et al., 2018; Gutiérrez et al., 2019), although the marginal bulges were not characterized quantitatively, nor explained from the mechanical perspective.

Moment forces associated with the development of a flexural depression may be accompanied by the formation of a marginal upward deflection or bulge by elastic deformation (Allen and Allen, 1992; Watts, 2001). This is a common phenomenon in lithospheric-scale elastic deformations. For instance, the vertical deflection of the lithosphere related to the built up of an orogenic wedge or volcanic islands, produces a subsidence depression and an outer flexural bulge with more limited extent and structural relief. In our case, the gravitational vertical stress that governs subsidence is not caused by an upper load, but by the lack of basal support.

Several geometrical and mechanical scenarios can be envisioned in which vertical bending-moment stress can be transferred from the subsidence zone to the marginal area of the sinkhole to produce a bulging ring (Fig. 8). The transference of these stresses largely depends on the rheology of the material (e.g., rigidity) and the mechanical coupling between the material affected by subsidence and the surrounding sediments. Flexural bulging may occur at the margins of a pure sagging structure (Fig. 8A). Sagging or passive bending involves the horizontal shortening of the deflected material, which in this case would be counterbalanced by continuous layer lengthening, preventing the decoupling between the subsiding material and the encasing sediments through the development of extensional fissures and faults at the margins. In sagging and collapse sinkholes with marginal vertical and outward dipping (i.e., antithetic) collapse faults with horizontal separation (i.e., dilation or heave), there is mechanical decoupling between subsiding and surrounding materials, preventing the transfer of moment-bending stresses and bulging development (Fig. 8B). This scenario B may correspond to an evolutionary stage following the scenario A, as sagging and the concomitant horizontal shortening progresses. Subsidence in collapse sinkholes bounded by vertical ring faults (piston-like structure) may generate drag folds and bulging of limited width at the margins (Fig. 8C).

The mechanical coupling between the foundering block and the encasing material may decrease as a progressively weaker fault zone develops by shearing. Fabregat et al. (2019), in a trench excavated at the margin of a collapse sinkhole, documented in the footwall of the steeply dipping collapse fault a drag fold in hardened alluvium with an associated bulge 1.3 m wide and 0.3 m in structural relief. In collapse sinkholes controlled by outward dipping faults (upright cone section) subsidence causes the complete mechanical decoupling between the foundering block and the surrounding material, which tends to experience inward flexing and or collapse due to lack of basal support (Poppe et al., 2015; Al-Halbouni et al., 2018; Fig. 8D). In the case of collapse sinkholes with inward dipping collapse faults (reversed cone section), the foundering block tends to pull-apart and rotate outwards and upwards the surrounding material, inducing flexural bulging (Fig. 8E). Data gathered by GPR and leveling on the internal structure of the Estrellas sinkhole indicates that the bulging recorded in this sinkhole may fit with a geometrical situation that combines scenarios A (sagging) and E (collapse with inward dipping faults). Marginal bulges are rarely observed in the geological record (paleosinkholes). This may be attributed to flexural recovery in the marginal bulge as moment-bending stresses drop by mechanical decoupling and/or subsidence cessation.

7.5. Boundary of the Estrellas sinkhole and active dissolution

Pre-existing active sinkholes concealed by anthropogenic filling and urban development are responsible for the great part of the subsidence damage in the mantled evaporite karst of the Ebro Valley (e.g., Galve et al., 2009; Desir et al., 2018), which is considered to be the karst region in Europe with the highest sinkhole risk (Gutiérrez et al., 2018). Consequently, identifying buried sinkholes and precisely mapping the edges of the areas affected by deformation is the main tasks for the application of preventive and corrective measures. Previous works based on the interpretation of old aerial photographs and detailed mapping of surface ruptures indicate a sinkhole around 100 m long (yellow line in Figure 9). However, all

the leveling lines reveal that ground deformation affects a significantly larger area (Fig. 9). For instance, in the northern leveling line, located in the central sector of the sinkhole, subsidence and uplift clearly affects a section 130 m long. This indicates that sinkhole mapping based on geomorphic criteria may significantly underestimate the actual extent of the area affected by ground displacement. A similar finding was presented by Gutiérrez et al. (2018) by comparing the extent of sinkholes with sagging subsidence identified via trenching, and the more restricted ones based on geomorphic and geophysical data.

The integration of the deformation data provided by the three non invasive techniques applied in this investigation allows mapping with a reasonable degree of confidence the boundary of the sinkhole deformation zone in a built-up area (purple line in Fig. 9). This boundary is based on the following information, in order of importance: (1) sections of the leveling lines unambiguously affected by vertical displacement (i.e., subsidence and uplift); (2) outermost mapped surface deformation features clearly attributable to sinkhole activity; and (3) limits of the subsidence structures imaged in the GPR profiles. In the sectors with insufficient or limited data, including the department store (building A), the boundary has been defined delineating a line parallel to the sinkhole edge mapped in 1996 by direct topographic surveying. The resulting map differentiates: (1) an inner rapidly deforming sector with subsidence rates higher than 0.8 cm/yr (blue line in Fig. 9); (2) an annular zone affected by slow subsidence (<0.8 mm/yr); and (3) a marginal ring that experiences slow uplift. Menezes et al. (2019), in a bare limestone karst area of Brazil, by using UAV-derived high-resolution digital elevation models of collapse sinkholes, identify marginal subsidence rings with poor geomorphic expression. These authors indicate that the consideration of this inward flexing zone leads to sinkhole radius around two times larger.

The proposed boundary of the Estrellas sinkhole has a minimum area of 11,824 m^2, omitting the portion underlying the department store, which means an increment of at least 6,320 m^2

(115%) with respect to the perimeter mapped in 1996 (Fig. 9). This new area, together with the mean subsidence rate recorded in the northern leveling line of 16.38 mm/yr (Table 1), yields a rough annual volumetric change of 194 m^3/yr. This value, which is comparable to those estimated with leveling data for other damaging sinkholes of the Ebro Valley (Logroño highway sinkhole: 276 m^3/yr; Pikolín sinkhole: 164 m^3/yr; Desir et al., 2018), can be considered as an approximate estimate of the amount of soluble rock dissolved annually at the sinkhole site. These high rates of long-sustained dissolution and subsidence must be related to the dissolution of high-solubility salts (i.e., halite, glauberite), as support the following lines of evidence: (1) Deep borehole data indicate that halite and glauberite units are expected in the bedrock underlying the alluvium at the sinkhole site (Salvany, 2009). Unfortunately, no boreholes reaching unweathered bedrock have been drilled in the central sector of the sinkhole. (2) Hydrochemical analyses of groundwater from the evaporitic aquifer collected at the adjacent pumping well indicate that they are saturated with respect to gypsum (Acero et al., 2013, 2015). Therefore, salt dissolution is needed to justify the large rate of mass depletion in the subsurface. (3) The rapid and significant reduction of the subsidence in building C following the closure of the pumping well points to a highly active and sensitive salt dissolution system.

8. Conclusions

The presented investigation, applying non-invasive methods, illustrates the strengths, drawbacks and complementarity of the different approaches for sinkhole characterization and monitoring in urban areas.

Detailed mapping of geomorphic features and surface deformation may lead to significant underestimates of the extent of the sinkhole area, but it is an essential preliminary task for designing the layout of site investigations and monitoring systems.

GPR is a suitable non-intrusive method for unravelling the internal structure of sinkholes in alluvial karst settings. This information provides the basis for identifying the subsidence mechanisms (i.e., sagging, collapse, suffosion), which are an essential aspect for risk assessment and mitigation. GPR profiles may be used to approximately delineate the boundaries of the subsidence areas, although there may be significant uncertainty in sagging sinkholes in which the edges are defined by subtle and gradual changes in the dip of stratigraphic markers. Generally, in urban areas, this geophysical approach is restricted to the use of shielded antennas with relatively high frequency, limiting the investigation depth. The quality of the information provided by the radargrams perpendicular to the deformation structures (e.g., tilted beds, collapse faults, fissures) is significantly higher than those with oblique orientation. Consequently, investigations with a radial layout may offer better results than those with an orthogonal arrangement.

High-precision leveling provides, over relatively short monitoring periods, highly useful information on critical aspects for the characterization of the deformation associated with active sinkholes affected by progressive displacement. It allows to precisely define the sections of the leveling lines affected by vertical displacement and the boundaries of the unstable area. In the case of the Estrellas sinkholes, leveling data indicates a deformation area much larger than that interpreted on the basis of old airborne imagery and surface-deformation mapping; radius around 30% larger and area over 2 times higher. The new outline of the sinkhole reveals that additional, previously unrecognized buildings, are affected by ground subsidence. Leveling data also allow resolving the spatial pattern of vertical deformation. In the analyzed sagging and collapse sinkhole, displacement data indicate an inner zone affected by rapid subsidence (>0.8 cm/yr), an outer ring characterized by slower settlement and with limited surface expression, and a marginal flexural bulge up to 30 m wide affected by slow uplift. The average uplift rate in the bulge is 3-5 times lower than the mean subsidence rate in the

corresponding leveling lines. To our knowledge, this is the first time that marginal uplift is characterized quantitatively in an active sinkhole. Probably, this is a common process that goes unnoticed because its identification requires the application of a high-precision geodetic method such as leveling. It is proposed that potential upward elastic deflection at the sinkhole margins is conditioned by factors such as the rigidity of the material affected by deformation and the mechanical coupling between the subsidence zone and the surrounding material. Strain rates provided by leveling can be also used to estimate the volume of soluble material removed from the subsurface annually and propose a karstification model in our case involving rapid salt dissolution. The main potential limitations of high-precision leveling include its limited spatial resolution, insufficient to resolve deformation associated with discrete structures (e.g., collapse faults), its limited practicality for sinkholes characterized by low-frequency episodic displacement, and the potential loss of benchmarks.

The data presented in this work shows that water pumping may have a large impact on the deformation rates associated with sinkholes related to highly sensitive salt dissolution systems. It also supports the concept that compaction grouting performed above voids and karstification zones may have a limited effectiveness or may even aggravate the problem.

The synergistic integration of the data gathered by the different methods, covering various deformation time scales, illustrates the suitability of combining the presented non-invasive, relatively cheap and simple-processing methods for the characterization of active sinkholes in urban areas.

Acknowledgements

This work has been supported by project CGL2017-85045-P (Ministerio de Ciencia, Innovación y Universidades, Gobierno de España). J.S. has a predoctoral contract (PRE2018-084240) cofinanced by the Spanish Government and the European Social Fund (ESF).

Declaration of interests

The authors declare that they have no known competing financial interests or personal relationships that could have appeared to influence the work reported in this paper.

References

Acero, P., Auqué, L.F., Galve, J.P., Gutiérrez, F., Carbonel, D., Gimeno, M. J., Yechieli, Y., Asta, M.P., Gómez, J.B. (2015). Evaluation of geochemical and hydrogeological processes by geochemical modeling in an area affected by evaporite karstification. Journal of Hydrology 529, 1874-1889.

Acero, P., Gutiérrez, F., Galve, J.P., Auqué, L.F., Carbonel, D., Gimeno, M. J., Gómez, J.B., Asta, M.P., Yechieli, Y. (2013). Hydrogeochemical characterization of an evaporite karst area affected by sinkholes (Ebro Valley, NE Spain). Geologica Acta 11(4), 389-407.

Al-Halbouni, D., Holohan, E.P., Taheri, A., Schöpfer, M.P.J., Emam, S., and Dahm, T. (2018). Geomechanical modelling of sinkhole development using distinct elements: model verification for a single void space and application to the Dead Sea area, Solid Earth 9, 1341–1373.

Allen, P.A., Allen, J.R. (1992). Basin analysis: Principles and application to petroleum play assessment. Blackwell, Oxford, 632 p.

Benito-Calvo, A., Gutiérrez, F., Martínez-Fernández, A., Carbonel, D., Karampaglidis, T., Desir, G., Sevil, J., Guerrero, J., Fabregat, I., García-Arnay, Á. (2018). 4D monitoring

of active sinkholes with a terrestrial laser scanner (TLS): a case study in the evaporite karst of the Ebro valley, NE Spain. Remote Sensing 10(4), 571.

Buurman, N., Reuther, C.D. (2006). Profiling of sinkholes in the metropolitan region of hamburg and Lüneburg with ground penetrating radar (GPR). Geophysical Research Abstract 8, 01878.

De Bruyn, I.A., Bell, F.G. (2001). The occurrence of sinkholes and subsidence depressions in the far West Rand and Gauteng province, South Africa, and their engineering implications. Environ. Eng. Geosci. 7(3), 281–295

De Giorgi, L., Leucci, G. (2014). Detection of hazardous cavities below a road using combined geophysical methods. Surveys in Geophysics 35(4), 1003-1021.

Desir, G., Gutiérrez, F., Merino, J., Carbonel, D., Benito Calvo, A., Guerrero, J., Fabregat, I. (2018). Rapid subsidence in damaging sinkholes: Measurements by high-precision leveling and the role of salt dissolution. Geomorphology 303, 393–409.

Dougherty, P. (2005). Sinkhole destruction of Corporate Plaza, Pennsylvania. In: Waltham T, Bell F, Culshaw M (Eds.). Sinkholes and subsidence. Springer, Chichester, 304–308

Fabregat, I., Gutiérrez, F., Roqué, C., Comas, X., Zarroca, M., Carbonel, D., Guerrero, J., Linares, R. (2017). Reconstructing the internal structure and long-term evolution of hazardous sinkholes combining trenching, electrical resistivity imaging (ERI) and ground penetrating radar (GPR). Geomorphology 285, 287-304.

Fabregat, I., Gutiérrez, F., Roqué, C., Zarroca, M., Linares, R., Comas, X., Guerrero, J., Carbonel, D. (2019). Subsidence mechanisms and sedimentation in alluvial sinkholes inferred from trenching and ground penetrating radar (GPR). Implications for subsidence and flooding hazard assessment. Quaternary International 525, 1-15.

Fischer, J.A., Fischer, J.J., Terry, J. (2018). Remediation of the centenary College President's House. In: Sasowsky, I.D., Byle, M.J., Land, L. (Eds.). Proceedings of the 15th

Multidisciplinary Conference on the Sinkholes and the Engineering and Environmental Impacts of Karst and the 3rd Appalachian Karst Symposium. National Cave and Karst Research Institute, 369-374.

Ford, D.C., Williams, P.W. (2007). Karst Hydrogeology and Geomorphology. Chichester, Wiley and Sons, 577 p.

Galve, J.P., Castañeda, C., Gutiérrez, F. (2015). Railway deformation detected by DInSAR over active sinkholes in the Ebro Valley evaporite karst, Spain, Nat. Hazards Earth Syst. Sci. 15, 2439–2448.

Galve, J.P., Gutiérrez, F., Lucha, P., Bonachea, J., Cendrero, A., Gimeno, M.J., Gutiérrez, M., Pardo, G., Remondo, J., Sánchez, J.A. (2009). Sinkholes in the salt-bearing evaporite karst of the Ebro River valley upstream of Zaragoza city (NE Spain). Geomorphological mapping and analysis as a basis for risk management. Geomorphology 108, 145–158.

Gołębiowski, T., Jarosińska, E. (2019). Application of GPR and ERT methods for recognizing of gypsum deposits in urban areas. Acta Geophysica, 1-16.

Goodings, D.J., Abdulla, W.A. (2002). Stability charts for predicting sinkholes in weakly cemented sand over karst limestone. Eng. Geol. 65:179–184

Guerrero, J., Gutiérrez, F., Galve, J.P. (2013). Large depressions, thickened terraces, and gravitational deformation in the Ebro River valley (Zaragoza area, NE Spain): evidence of glauberite and halite interstratal karstification. Geomorphology 196, 162–176.

Gutiérrez, F., Benito-Calvo, A., Carbonel, D., Desir, G., Sevil, J., Guerrero, J., Martínez-Fernández, A., Karamplaglidis, T., García-Arnay, Á., Fabregat, I. (2019). Review on sinkhole monitoring and performance assessment of the performance of remediation measures by high-precision leveling and terrestrial laser scanner in the salt karst of the Ebro Valley, Spain. Engineering Geology 248, 283-308.

Gutiérrez, F., Galve, J.P., Lucha, P., Bonachea, J., Jordá, L., Jordá, R. (2009). Investigation of a large collapse sinkhole affecting a multi-storey building by means of geophysics and the trenching technique (Zaragoza city, NE Spain). Environmental Geology, 58(5), 1107-1122.

Gutiérrez, F., Guerrero, J., Lucha, P. (2008). A genetic classification of sinkholes illustrated from evaporite paleokarst exposures in Spain. Environmental Geology 53(5), 993-1006.

Gutiérrez, F., Parise, M., De Waele, J., Jourde, H. (2014). A review on natural and human induced geohazards and impacts in karst. Earth-Sci. Rev. 138, 61–88.

Gutiérrez, F., Zarroca, M., Linares, R., Roqué, C., Carbonel, D., Guerrero, J., James, P., McCalpin, J.P., Comas, X., Cooper, A.H. (2018). Identifying the boundaries of sinkholes and subsidence areas via trenching and establishing setback distances. Engineering Geology 233, 255-268.

Intrieri, E., Gigli, G., Nocentini, M., Lombardi, L., Mugnai, F., Fidolini, F., Casagli, N. (2015). Sinkhole monitoring and early warning: an experimental and successful GBInSAR application. Geomorphology 241, 304–314.

ISO 17123-2. (2001). Optics and optical instruments. Field procedures for testing geodetic and surveying instruments. Part 2: Levels. Geneva, Switzerland, 14 p.

Jassim, S.Z., Jibril, A.S., Numan, N.M.S. (1997). Gypsum karstification in the Middle Miocene Fatha Formation, Mosul area, northern Iraq. Geomorphology 18, 137–149

Kersten, T., Kobe, M., Gabriel, G., Timmen, L., Schön, S., Vogel, D. (2017). Geodetic monitoring of subrosion-induced subsidence processes in urban areas. Journal of Applied Geodesy 11, 21–29

Kobe, M., Gabriel, G., Weise, A., Vogel, D. (2019). Time-lapse gravity and levelling surveys reveal mass loss and ongoing subsidence in the urban subrosion-prone area of Bad Frankenhausen, Germany. Solid Earth 10(3), 599-619.

Kruse, S., Grasmueck, M., Weiss, M., Viggiano, D. (2006). Sinkhole structure imaging in covered karst terrain. Geophysical Research Letters 33(16).

Lei, M., Jiang, X., Guan, Z. (2013). Emergency investigation of extremely large sinkholes, Maohe, Guangxi, China. In: L. Land, D. H. Doctor, J. B. Stephenson (Eds.), Sinkholes and the engineering and environmental impacts of karst (pp. 145–151). Carlsbad, NM: National Cave and Karst Research Institute.

Menezes, D.F., Bezerra, F.H., Balsamo, F., Arcari, A., Maia, R.P., Cazarin, C.L. (2019). Subsidence rings and fracture pattern around dolines in carbonate platforms – Implications for evolution and petrophysical properties of collapse structures. Marine and Petroleum Geology, 104113.

Poppe, S., Holohan, E.P., Pauwels, E., Cnudde, V., Kervyn, M. (2015). Sinkholes, pit craters, and small calderas: Analog models of depletion-induced collapse analyzed by computed X-ray microtomography. Bulletin 127(1-2), 281-296.

Pueyo-Anchuela, Ó., Juan, A.P., Casas Sainz, A.M., Ansón-López, D., Gil-Garbi, H. (2013). Actual extension of sinkholes. Considerations about geophysical, geomorphological, and field inspection techniques in urban planning projects in the Ebro basin (NE Spain). Geomorphology 189, 135-149.

Pueyo-Anchuela, Ó., López, D.A., Juan, A.P., Sainz, A.M.C., Simón, J.L., Gil, H., Ipas-Llorens, J.F., Abadías, J.G. (2012). Consideraciones sobre la construcción en zonas kársticas activas. Caso de la Avenida de las Estrellas de Zaragoza. Geogaceta 51, 63-66.

Quirantes, J. (1978) Estudio sedimentológico y estratigráfico del Terciario continental de los Monegros. Instituto Fernando el Católico, CSIC, Zaragoza, Spain, 208 p.

Rodríguez, V., Gutiérrez, F., Green, A.G., Carbonel, D., Horstmeyer, H., Schmelzbach, C. (2014). Characterising sagging and collapse sinkholes in a mantled karst by means of Ground Penetrating Radar (GPR). Environ. Eng. Geosci. 20, 109–132.

Ronen, A., Ezersky, M., Beck, A., Gatenio, B., Simhayov, R.B. (2019). Use of GPR method for prediction of sinkholes formation along the Dead Sea Shores, Israel. Geomorphology 328, 28-43.

Salvany, J.M. (2009). Geología del Yacimiento Glauberítico de Montes de Torrero. Universidad de Zaragoza, Zaragoza, Spain, 80 p.

Salvany, J.M., García-Veigas, J., Ortí, F. (2007). Glauberite-halite association of the Zaragoza Gypsum Formation (Lower Miocene, Ebro Basin, NE Spain). Sedimentology 54, 443–467.

Sandmeier, K.J. (2019). REFLEX. Version 9.0. Sandmeier Software ZipserStrabe1. D-76227 Karlsruhe, Germany.

Sevil, J., Gutiérrez, F., Zarroca, M., Desir, G., Carbonel, D., Guerrero, J., Linares, R., Roqué, C., Fabregat, I. (2017). Sinkhole investigation in an urban area by trenching in combination with GPR, ERT and high-precision leveling. Mantled evaporite karst of Zaragoza city, NE Spain. Engineering Geology 231, 9-20.

Simón, J.L., Martínez-Gil, F.J., Soriano, M.A., Arlegui, L.E., Caballero, J. (1998). Plan general de ordenación urbana. Anejo 3. Estudios Geológicos-Geotécnicos., Ayuntamiento de Zaragoza, Spain.

Wadas, S.H., Tanner, D.C., Polom, U., Krawczyk, C.M. (2017). Structural analysis of S-wave seismics around an urban sinkhole: evidence of enhanced dissolution in a strike-slip fault zone. Natural Hazards and Earth System Sciences 17(12), 2335.

Watts, A.B. (2001). Isostasy and Flexure of the Lithosphere. Cambridge University Press, 480 p.

Witze, A. (2013). Florida forecasts sinkhole burden. Nature News, 504(7479), 196.

Zarroca, M., Comas, X., Gutiérrez, F., Carbonel, D., Linares, R., Roqué, C., Mozafari, M., Guerrero, J., Pellicer, X.M. (2017). The application of GPR and ERI in combination with exposure logging and retrodeformation analysis to characterize sinkholes and reconstruct their impact on fluvial sedimentation. Earth Surf. Process. Landf. 42, 1049–1064.

Figure captions:

Figure 1. Geographic and geomorphological setting of the Estrellas sinkhole. (A) Location of the Ebro Cenozoic Basin (light area south of the Pyrenees) and Zaragoza city in NE Spain. (B) Shaded relief model of a stretch of the Ebro River valley showing the location of the investigated site and relevant deep boreholes mentioned in the text. Images A and B from the Spanish National Geographic Institute. (C) Geomorphological map illustrating the geomorphic context of the Estrellas sinkhole on the southern margin of the Ebro Valley and in the southwestern sector of Zaragoza city.

Figure 2. Aerial and satellite imagery illustrating the recent evolution of the sinkhole site. (A) Photogrammetric orthoimage from 1927 showing the sinkhole on a bare terrace surface. The continuous black line corresponds to a contour line. (B) Aerial photograph from 1956. The dashed line depicts the edge of the enclosed depression interpreted under the stereoscope. (C) Aerial photograph from 1993 showing a factory built on the NE sector of the sinkhole. The portion of the factory overlying the sinkhole was demolished. The dark band is an asphalt cover placed on marginal scarps and fissures of the sinkhole. (D) Orthoimage from 2019 illustrating the current situation with the sinkhole located in an urbanized area. The solid line indicates the georeferenced outline of the sinkhole mapped by the company ENTECSA in 1996. The central

sector of the sinkhole is occupied by a sloping red clay cap installed to reduce water infiltration. The images do not share the same scale.

Figure 3. Surface deformation map showing the distribution of the buildings associated with the Estrellas sinkhole and the layout of the leveling lines, which essentially coincide with the distribution of the GPR profiles. Map produced on 2 August 2017. The figure includes the sinkhole perimeters proposed by previous authors and the expansion joints that subdivide building C into five blocks. The outline of Simón et al. (1998) has been reproduced from Pueyo-Anchuela et al. (2012). Coordinate system: ETRS89 Zone 30N.

Figure 4. Images of subsidence damage and features associated with the Estrellas sinkhole. A: Top of expansion joint between the blocks C5-C4 in the southern side of building C showing a primary joint-normal displacement and a secondary joint-parallel movement. Photograph taken on March 2008. B: Sidewalk next to building A tilted and detached from the façade. Photograph taken on May 2014. C: Collapse depression around 1 m across occurred at the southeastern corner of the central square in May 2015. Arrows point to the outer cracks. D: Collapse around 30 cm long formed next to the northeastern corner of building D in June 2017. E: Intersection between the Estrellas St. and Algenib St. before its re-pavement and scarp of the NW sector of the sinkhole. F: Covered expansion joint between blocks C5-C4 in the southern side and rooftop of building C, showing both joint-normal and joint-parallel relative displacement. G: Repaired west-facing scarp and fissure at the western sector of the basement of the building C. Arrows point to the expansion joint between the blocks C4-C3. Photograph E taken on October 2018, F and G on August 2019.

Figure 5. Comparison of the deformation map, showing the distribution of the Estrellas Sinkhole North leveling line and the coincident GPR profiles. A: Excerpt of the surface deformation map showing the layout of the leveling line and the GPR profiles. Red and green rectangles indicate the sections clearly affected by subsidence and uplift, respectively, as defined by the last complete deformation profile. B, C and D: GPR profiles gathered along the southern and northern sides of the Estrellas street with 100 MHz and 200 MHz shielded antennas. The red lines indicate the position of faults/fractures inferred from laterally truncated reflections. The orange triangles mark the limits of the subsidence structure (unfilled triangles when unclear). E: Cumulative vertical displacement profiles constructed with the leveling data acquired between 24/01/2017 and 15/05/2019.

Figure 6. Comparison of the deformation map showing the distribution of the Estrellas Sinkhole West leveling line and the adjacent GPR profiles acquired along the Algenib Street. A: Extract of the surface deformation map showing the layout of the leveling line and the GPR profiles. In this case the whole leveling line experiences continuous active subsidence. B and C: GPR profiles gathered along the Algenib Street with 100 MHz and 200 MHz shielded antennas. The red lines indicate the location of faults/fractures inferred from laterally truncated reflectors. The orange triangles point to the limits of the subsidence structure; unfilled triangles when unclear. The northern boundary lies below the department store. D: Cumulative displacement profile created with the leveling data acquired between 24/01/2017 and 15/05/2019.

Figure 7. Comparison of the deformation map, the GPR and the high-precision leveling data collected along the eastern part of sinkhole, i.e., Capella Street. A: Simplification of the surface

deformation map showing the layout of the leveling line and the GPR profiles. The red rectangle indicates the section of continuous active subsidence detected by the high-precision leveling. B and C: GPR profiles gathered along the Capella Street with 100 MHz and 200 MHz shielded antennas. The red lines mark fractures represented as laterally truncated reflectors, and the blue arrows mark the location of major diffraction hyperbolae. There is a yellow line in the 100 MHz profile indicating the angular unconformity detected along the majority of the GPR profile. The orange triangles point to the limits of the subsidence structure, unfilled unclear. The northern boundary lies below the department store. E. Cumulative displacement profile created with the leveling data acquired in the eastern section of the Estrellas sinkhole between 24/01/2017 and 15/05/2019.

Figure 8. Schematic representation of geometrical and rheological subsidence scenarios with mechanical coupling or decoupling between the subsidence zone and the surrounding material and the development of marginal bulges (A, C, E).

Figure 9. Orthoimage of the study area showing the perimeter proposed for the Estrellas Sinkhole based on the integration of the data gathered through mapping, high-precision leveling, and GPR. The boundary of the sinkhole mapped by ENTECSA in 1996 before the construction of the building A has also been considered. See explanation in the text. Coordinate system: ETRS89 Zone 30N.

Table 1. Summary of the leveling data gathered in the Estrellas Sinkhole North line. The parameters are described in the text.

	Estrellas Sinkhole North									
Measurement dates	24/01/2017	26/04/2017	20/07/2017	25/09/2017	15/12/2017	16/03/2018	29/06/2018	12/11/2018	12/02/2019	15/05/2019
Measurement period (days)		92	177	244	325	416	521	657	749	841
Lenght of line (m)	200									
Benchmarks recording subsidence		10	13	14	16	14	15	16	16	12
Lenght affected by subsidence (m)		45	60	65	75	65	70	75	75	60
Mean cumulative subsidence (mm)		-1.524	-5.344	-9.189	-14.623	-18.327	-21.916	-27.259	-33.602	-32.692
Maximum cumulative subsidence (mm)		-2.530	-8.900	-15.265	-24.320	-28.905	-36.535	-47.725	-59.100	-57.700
Mean subsidence rate (mm/yr)		-6.046	-11.026	-13.745	-16.423	-16.080	-15.354	-15.144	-16.375	-14.188
Maximum subsidence rate (mm/yr)		-10.038	-18.353	-22.835	-27.313	-25.361	-25.596	-26.514	-28.800	-25.042
Mean cumulative uplift (mm)		2.403	3.535	3.613	2.318	5.108	4.502	4.473	6.074	5.124
Maximum cumulative uplift (mm)		4.795	6.265	6.180	3.955	9.155	7.345	7.500	12.135	7.930
Mean uplift rate (mm/yr)		9.536	7.290	5.405	2.604	4.482	3.154	2.485	2.960	2.224
Maximum uplift rate (mm/yr)		19.024	12.919	9.245	4.442	8.033	5.146	4.167	5.914	3.442
Mean kilometric error (mm/km)	0.0033									
Asymmetry index	1.147									
Eccentricity index	0.813									
Subsidence geometry index	1.759									

Table 2. Summary of the leveling data gathered along the western leveling line of the Estrellas sinkhole. The parameters are described in the text.

	Estrellas Sinkhole West									
Measurement dates	24/01/2017	25/04/2017	20/07/2017	25/09/2017	15/12/2017	20/03/2018	29/06/2018	12/11/2018	05/02/2019	15/05/2019
Measurement period (days)		91	177	244	325	420	521	657	742	841
Lenght of line (m)	85									
Benchmarks recording subsidence		10	16	17	17	17	17	17	17	13
Lenght affected by subsidence (m)		50	80	85	85	85	85	85	85	65
Mean cumulative subsidence (mm)		-3.907	-5.946	-7.746	-	- 13.109	- 16.330	- 20.394	- 26.427	- 25.400
Maximum cumulative subsidence (mm)		-7.040	- 29.055	-	-	- 34.040	- 41.615	- 52.315	- 67.510	- 77.555
Mean subsidence rate (mm/yr)		- 15.671	-	- 11.587	- 12.929	- 11.393	- 11.441	- 11.330	- 13.000	- 11.024
Maximum subsidence rate (mm/yr)		- 28.237	-	- 51.915	- 48.935	- 29.582	- 29.154	- 29.064	- 33.209	- 33.659
Mean kilometric error (mm/km)	0.0013									

Table 3. Summary of the leveling data gathered in the eastern leveling line of the Estrellas sinkhole. The parameters are described in the text.

	Estrellas Sinkhole East									
Measurement dates	24/01/ 2017	26/04/ 2017	20/07/ 2017	25/09/ 2017	15/12/ 2017	16/03/ 2018	29/06/ 2018	12/11/ 2018	12/02/ 2019	15/05/ 2019
Measurement period (days)		92	177	244	325	416	521	657	749	841
Lenght of line (m)	95									
Benchmarks affected by subsidence		0	8	4	6	13	9	10	10	14
Lenght affected by subsidence (m)		0	40	20	30	65	45	50	50	65
Mean cumulative subsidence (mm)		0	-0.636	-0.209	-0.901	-1.831	-2.717	-2.969	-3.220	-3.176
Maximum cumulative subsidence (mm)		0	-1.275	-0.405	-1.651	-2.505	-2.905	-3.704	-3.980	-5.790
Mean subsidence rate (mm/yr)		0	-1.312	-0.312	-1.012	-1.607	-1.903	-1.650	-1.569	-1.379
Maximum subsidence rate (mm/yr)		0	-2.629	-0.606	-1.855	-2.198	-2.035	-2.058	-1.940	-2.513
Mean cumulative uplift (mm)		0.504	0.585	0.779	0.723	0.395	0.928	1.457	0.773	1.009
Maximum cumulative uplift (mm)		0.850	0.860	1.440	1.585	0.680	1.730	3.050	2.230	2.275
Mean uplift rate (mm/yr)		2.000	1.206	1.165	0.812	0.347	0.650	0.809	0.376	0.438
Maximum uplift rate (mm/yr)		3.372	1.773	2.154	1.780	0.597	1.212	1.694	1.087	0.987
Mean kilometric error (mm/km)	0.0017									

Highlights

- Multimethod and non-invasive investigation of a sinkhole in an urban area.
- The studied sinkhole has caused direct losses higher than 15 Meuro.
- Spatial-temporal deformation patterns revealed by high-precision leveling and GPR.
- Quantitative characterization of marginal uplift in an active sinkhole.
- Assessment of the performance of sinkhole mitigation measures.